Journal of Geophysical Research: Oceans

RESEARCH ARTICLE
10.1029/2018JC014290

Key Points:
- Anticyclonically sheared flank jets strongly affect the patterns of larval dispersal at the EPR 9–10°N segment
- The effect of larval precompetency period on connectivity depends on the spacing of vent fields and advection in flank jets
- Transform faults and other topographic features on or near the ridge segment act as barriers to the along-ridge larval dispersal

Supporting Information:
- Supporting Information S1
- Movie S1
- Movie S2
- Movie S3
- Data Set S1

Correspondence to:
G. Xu,
guangyux@uw.edu

Citation:
Xu, G., McGillicuddy, D. J., Jr., Mills, S. W., & Mullineaux, L. S. (2018). Dispersal of hydrothermal vent larvae at East Pacific Rise 9–10°N segment. *Journal of Geophysical Research: Oceans*, *123*, 7877–7895. https://doi.org/10.1029/2018JC014290

Received 22 JUN 2018
Accepted 8 OCT 2018
Accepted article online 15 OCT 2018
Published online 6 NOV 2018

Dispersal of Hydrothermal Vent Larvae at East Pacific Rise 9–10°N Segment

Guangyu Xu[1], D. J. McGillicuddy Jr.[2], S. W. Mills[3], and L. S. Mullineaux[3]

[1]Applied Physics Laboratory, University of Washington, Seattle, WA, USA, [2]Applied Ocean Physics and Engineering Department, Woods Hole Oceanographic Institution (WHOI), Woods Hole, MA, USA, [3]Biology Department, WHOI, Woods Hole, MA, USA

Abstract A three-dimensional, primitive-equation, ocean circulation model coupled with a Lagrangian particle-tracking algorithm is used to investigate the dispersal and settlement of planktonic larvae released from discrete hydrothermal habitats on the East Pacific Rise segment at 9–10°N. Model outputs show that mean circulation is anticyclonic around the ridge segment, which consists of a northward flow along the western flank and a southward flow along the eastern flank. Those flank jets are dispersal expressways for the along-ridge larval transport and strongly affect its overall direction and spatial-temporal variations. It is evident from model results that the transform faults bounding the ridge segment and off axis topography (the Lamont Seamount Chain) act as topographic barriers to larval dispersal in the along-ridge direction. Furthermore, the presence of an overlapping spreading center and an adjacent local topographic high impedes the southward along-ridge larval transport. The model results suggest that larval recolonization within ridge-crest habitats is enhanced by the anticyclonic circulation around the ridge segment, and the overall recolonization rate is higher for larvae having a short precompetency period and an altitude above the bottom sufficient to avoid influence by the near-bottom currents Surprisingly, for larvae having a long precompetency period (>10 days), the prolonged travel time allowed some of those larvae to return to their natal vent clusters, which results in an unexpected increase in connectivity among natal and neighboring sites. Overall, model-based predictions of connectivity are highly sensitive to the larval precompetency period and vertical position in the water column.

Plain Language Summary In this study, we use state-of-the-art computer simulations to investigate how ocean currents transport larvae of animals living in hydrothermal vent fields on the crest of the East Pacific Rise ridge located at over 2,000 m below the surface of the Northeast Pacific. Our study provides an in-depth look into how currents, seafloor topography, and physiological traits of larvae influence the biological connectivity among different habitats on a segment of the East Pacific Rise. Our simulations suggest that ocean currents form a clockwise circulation around the ridge segment, which consists of a northward flow along the western flank and a southward flow along the eastern flank. Those flows, which we call flank jets, are expressways for larval transport along the ridge and largely control the overall direction of that transport. Our simulations also suggest that large faults at the ends of the ridge segments disrupt the movement of larvae along the ridge and reduce their chance of reaching habitats located on adjacent segments. On the other hand, the presence of the clockwise circulation enhances larval connectivity among habitats within the same segment, especially for larvae that mature quickly and spend their lifetime at higher altitudes above the seafloor.

1. Introduction

Hydrothermal vents support unique chemosynthetically based ecosystems. Those habitats are typically limited in area and geographically isolated. The benthic organisms living at a vent site are subject to local extinction caused by disturbance events (e.g., seafloor eruptions). For example, a vent may become uninhabitable through burial by lava or alteration of vent fluid conduits during a seafloor eruption. Since the adults of most benthic vent species are sessile and have very limited mobility, having a planktonic larval stage is therefore critical for connecting spatially disjoint populations and colonizing new habitats. Larval connectivity allows vent populations to persist regionally, despite the transience of their habitat, and influences the biodiversity and resilience of vent communities.

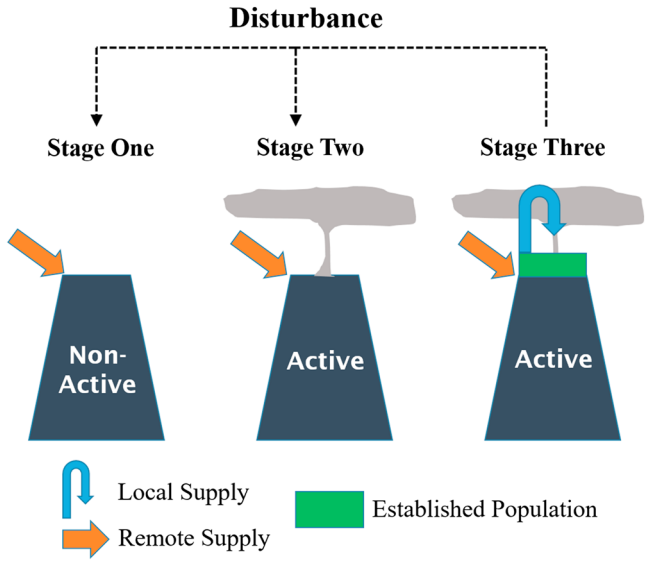

Figure 1. Conceptual diagram showing the stages of a hydrothermal habitat, as it progresses from dormancy (stage 1), to active but uninhabited (stage 2), to active, inhabited (stage 3), and then back to being uninhabited (stage 1 or 2) after a disturbance. The arrow type indicates the source of larval supply (local or remote).

The larvae of most vent species are small and have limited swimming capabilities. Therefore, the dispersal of vent larvae may be influenced strongly by ocean currents. The majority of hydrothermal habitats are located along mid-ocean ridges, atop seamounts, or in arc or back-arc basins, where the interaction between abyssal flows and rugged topography provides a potential for complex patterns of local circulation. In addition to ocean currents, the dispersal of a vent larva is also dependent on its swimming behavior and developments in its planktonic stage. Despite being weak swimmers, larval invertebrates may alter their dispersal distance and direction by changing their position above the seafloor in a vertically sheared flow field (e.g., as reviewed for coastal species in Shanks, 1995). A larva can change its vertical position through swimming, floating, and sinking. In a vent habitat, a larva can also elevate its vertical position via entrainment into a rising hydrothermal plume (Kim et al., 1994; Mullineaux & France, 1995). The major life history traits that affect larval dispersal include planktonic larval duration (PLD) and precompetency period (Tp). The former is the maximum time a larva can survive in its planktonic stage; the latter is the initial development time during which a larva matures and becomes capable to settle. Both parameters are largely unknown for most vent species. One exception is the tubeworm *Riftia pachyptila*, whose larvae have been cultured to obtain an estimated PLD of 30 to 40 days (Marsh et al., 2001). The settlement behavior of vent larvae after their Tp is also poorly understood but must involve encounter of suitable habitat to be successful.

Colonization of vents depends not only on the dynamics of larval supply but also on dynamics of the vents themselves. Vent habitat may be described as existing in one of three stages (Neubert et al., 2006; Figure 1). In the first stage (dormant) there is no active venting or benthic community. This situation occurs at a site that has temporarily ceased venting, or at a new site where venting has not yet occurred. The larval supply is purely from remote sources, but there is no larval settlement due to the absence of suitable habitat. In the second stage (active but uninhabited), hydrothermal venting resumes and larvae from remote sources are able to colonize the now-suitable habitat (e.g., Mullineaux et al., 2010). The ability of a species to colonize will depend on having a suitably long PLD to reach the newly suitable site, so studies of larval dispersal at vents typically incorporate PLD as a key factor (e.g., Mitarai et al., 2016; Vic et al., 2018). Once the local community is established, the habitat transitions to a third stage (active and inhabited) in which larval supply may come from either the local vent, or remote vents. In this third stage, larval Tp becomes important, as it influences the ability of a species to recolonize natal or neighboring sites. Field studies of larval supply suggest that local supply may dominate in some communities (Metaxas, 2004; Mullineaux et al., 2005), whereas supply from neighboring vents may dominate in others (Adams & Mullineaux, 2008). The established community persists until it is eradicated by another disturbance that transitions the site back to stage 1 or 2.

This concept of vent transitions provides a framework for our study, in which we use a numerical model to investigate the dispersal and settlement of larvae from a group of established vent communities (stage 3) on the East Pacific Rise (EPR) near 9°N. Our model simulates the dispersal of a large number of larvae spawned along the ridge crest in a three-dimensional (3-D) flow field over realistic ridge topography. Our approach is to examine how the complex ocean currents and topography near the ridge segment influence larval dispersal, retention, and connectivity and their sensitivity to larval life history traits (PLD and Tp) and behaviors. Numerical models were used to investigate larval dispersal at the EPR 9°–10°N in a couple of previous studies. Marsh et al. (2001) modeled the movement of larvae in a spatially homogeneous flow field derived from the measurements of a current meter deployed at 175 m above the ridge crest near the Biovent site (Figure 2c). Their results suggest that the along-ridge dispersal distance of the larvae of the tubeworm *R. pachyptila* is limited to 100 km along the direction of the ridge over a 30- to 40-day lifespan. More recently, McGillicuddy et al. (2010) used a two-dimensional (2-D) implementation of the model used in the current study to investigate the dispersal of larvae in a flow field that is spatially heterogeneous in the cross-ridge direction over an idealized infinitely long axisymmetric ridge. Their results suggested dispersal and retention of larvae depend

strongly on their vertical positions in the water column and Tp. In this study, we expand upon the work of McGillicuddy et al. (2010) to construct a fully 3-D simulation that implements realistic bathymetry to accommodate along axis variations of hydrodynamics. The 3-D model allows us to examine, for the first time, the larval dispersal at the EPR 9°–10°N in an explicitly expressed 3-D flow regime and realistic bathymetric setting. The explicit representation of discrete vent habitats in the 3-D model also permits detailed analysis of the larval connectivity of those habitats.

The ecological component of our study addresses two specific unresolved issues: the relative importance of local and remote larval supply at established vents and the potential for discontinuities in ridge topography, such as transform faults to function as barriers to larval connectivity. Specifically, we investigate how larval traits such as vertical positioning, planktonic duration, and Tp influence connectivity between vent fields in the 9°–10°N region of the EPR. Field observations of currents are used to inform the hydrodynamic model, and observations of larval supply at two selected vent sites whose communities differ in species composition are used for comparison with modeled larval connectivity.

Section 2 introduces the geological setting of the EPR 9°–10°N, its local vent habitats, and the previously observed eruption-induced disturbance to biological communities. Section 3 introduces the configuration of the numerical model and sediment-trap sample analysis. Section 4 discusses the simulated flow field near the ridge segment. Sections 5 to 7 show the simulated larval dispersal patterns and discuss noticeable hydrodynamic and topographic influences on larval transport. Section 8 compares the simulated larval supplies with the observations at two vent sites, which sheds light on the relative importance of local and remote larval supply at the EPR 9°–10°N. Section 9 discusses larval connectivity among the ridge-crest vent sites based on model results, followed by concluding remarks given in section 10 and a discussion of the implications of model results for long-distance larval dispersal in section 11.

2. Study Site

The EPR 9°–10°N is a fast-spreading ridge segment with a full spreading rate of ~110 mm/yr (Carbotte & Macdonald, 1994). The segment is bounded in between two transform faults: Clipperton in the north and Siqueros in the south (Figure 2a). The depth of the ridge crest reaches ~2,500 m. The abundant subsurface lava supply supports vigorous hydrothermal venting along the ridge crest. In this study, we focus on 10 major vent sites and divide those vents into three vent clusters (Figure 2c). The northern cluster includes the northernmost five vents: Biovent, EastWall, Bio9, Choo-Choo, and TevniaHole, where the 2006 eruption caused substantial perturbation to local communities. The middle cluster includes three adjacent vents to the south of the Northern cluster (V, A, and Hot8), which were not eradicated by the 2006 eruption. The Southern cluster includes the southernmost two vents in our study area: K and PBR500.

Vent environments at the EPR subject to regular disruption by volcanic events on decadal time scales (Perfit & Chadwick, 1998). At the 9°–10°N segment, there have been two documented seafloor eruptions, which occurred in 1991 (Haymon et al., 1993) and 2006 (Tolstoy et al., 2006). During the latter eruption, whose timing is estimated to be from late 2005 to January 2006 (Tolstoy et al., 2006), the lava flow that emerged between 9°46′ and 9°56′N eradicated local vent communities (Soule et al., 2007). Field observations of larval supply detected a striking change in species composition of larvae and colonists following the eruption, which is marked by the appearance of an immigrant species from hundreds of kilometers away and disappearance of several previously abundant local species (Mullineaux et al., 2010). Furthermore, long-term monitoring of communities at disturbed and undisturbed vent sites observed substantial effects of the posteruption arrival of species from remote locales (Mullineaux et al., 2012).

3. Methods

3.1. Sediment-Trap Sample Analysis

Larvae were collected in McLane PARFLUX Mark 78H-21 time series sediment traps with a 0.5-m^2 collecting area and 21 sequentially sampling cups. Downward-moving particles, including larvae, drop into the collection cups, which are filled with 20% dimethyl sulfoxide in saturated salt solution as a preservative (Khripounoff et al., 2000). The traps were positioned near vents in the Northern cluster, south of Bio9, and Southern cluster, north of K-vent, on autonomous subsurface moorings, with the trap opening positioned

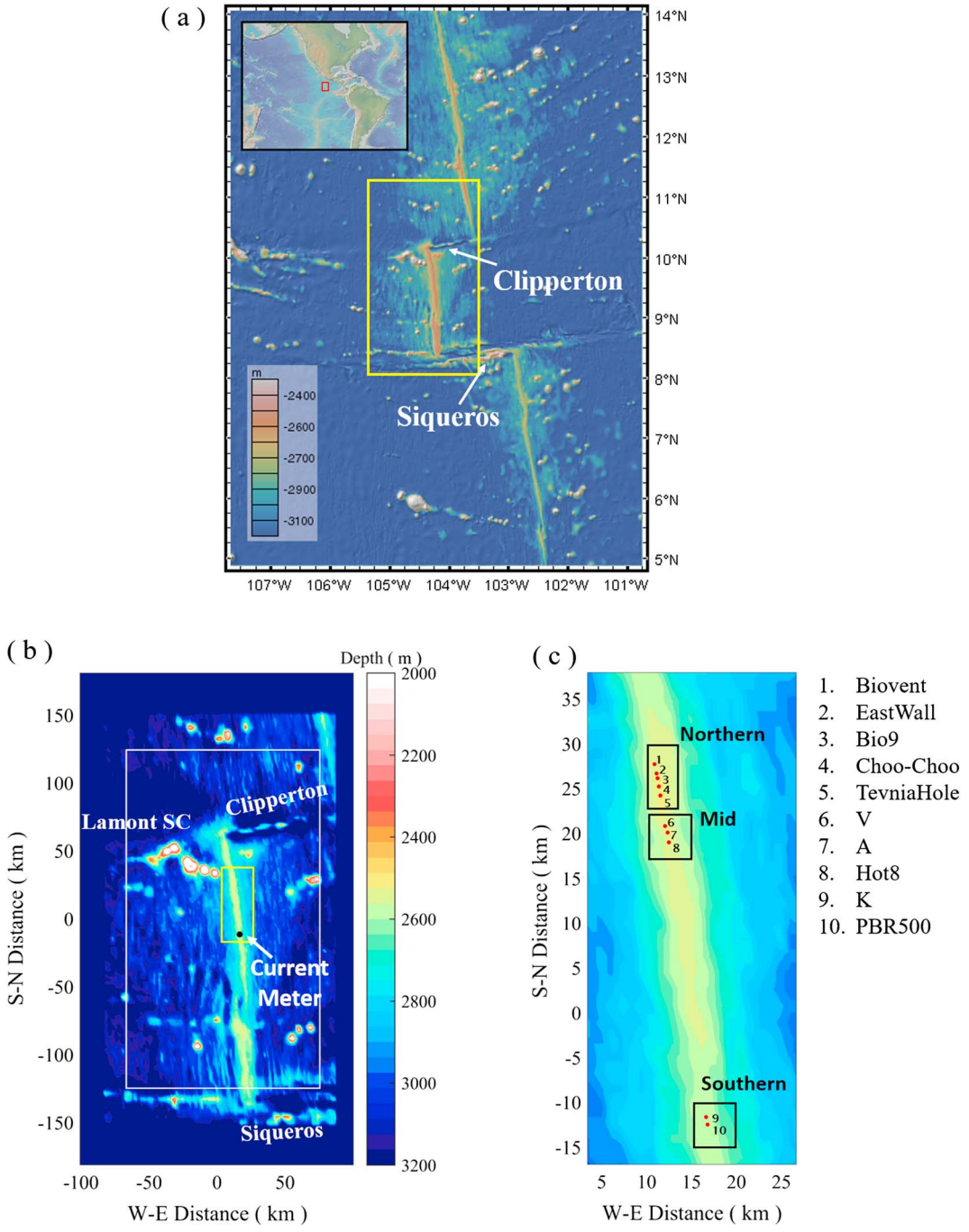

Figure 2. (a) Bathymetry of the East Pacific Rise between 5°N and 14°N (image generated using GeoMapApp: http://www.geomapapp.org, bathymetric data from Global Multi-Resolution Topography (Ryan et al., 2009)). The yellow box delimits the model domain shown in (b). The locations of the Clipperton and Siqueros transform faults (TFs) are labeled. (b) Bathymetry within the model domain. The white line marks the inner edge of the "pretty good sponge" (Lavelle & Thacker, 2008) zone used to absorb the waves generated in the model interior. The black dot indicates the location of a current meter deployed at 2,440 m depth from November 2006 to November 2007. The locations of the Clipperton and Siqueros TFs and the Lamont Seamount Chain are labeled. The coordinate origin is located at 10.00°N, 104.63°W. (c) Zoom-in view of the area within the yellow box in (b). The red dots mark the locations of 12 vent sites on the ridge crest. Those vent sites are numbered from north to south, and their names are listed on the right. The black boxes mark three vent clusters: northern, middle, and southern.

at 4 m above the bottom (Figure 2c). In each case, the trap was located directly in the axial trough within 200 m of an active vent. The traps sampled on a synchronized 14.8-day period, corresponding to the semilunar tidal cycle, between 17 November 2006 and 23 September 2007.

On recovery, samples from the trap cups were maintained at approximately 4 °C until the larvae were sorted and identified morphologically under a dissecting microscope to the lowest taxonomic level possible. Most shelled larvae, such as gastropods, were identified to the species level (Mills et al., 2009), but poor preservation of some other soft-bodied taxa (e.g., polychaetes) impeded their identification. Only individuals that were identified reliably to a vent taxon were in included in subsequent analyses. In cases where a portion of the sample was split off and used for geochemical analysis (i.e., for the northern trap, as described in Adams et al., 2011), larval counts in the remaining split were adjusted to compensate. Because the traps collect larvae that are swimming or sinking downward, flux of larvae into the trap is considered an indicator of larval supply to the benthos (Beaulieu et al., 2009; Todd et al., 2006).

We chose these sites for larval sampling because they differed in the number and proximity of neighboring vent communities (Figure 2c) and were expected to differ in patterns of hydrodynamically mediated larval connectivity. We wished to investigate how well the temporal patterns in total larval supply corresponded to estimates produced by the numerical model at the two sites. Although the samples revealed a broad diversity of mollusk species (see Table S1 in supporting information), the number of site-specific species (i.e., those found only at the northern or southern clusters) was too low for their patterns to be informative. Similarly, the numbers of individuals of the few species whose Tp could be estimated, for example, the mussel *Bathymodiolus thermophilus*, were too low for statistical analysis of temporal patterns. Therefore, larval abundances were pooled across species and the temporal analyses conducted on the total numbers of larvae collected in each time period. When comparing with model outputs, the 18 samples taken from December 2006 to October 2007 were pooled into 9 bins, each representing the total number of larvae collected during a 29- to 30-day period.

3.2. Model Design and Configuration

The numerical model used to investigate the dispersal of larvae along the EPR 9°–10°N is the ocean circulation model described in Lavelle et al. (2010) coupled with the Lagrangian particle tracking algorithm developed by Blanton (1995). In essence, the particle-tracking model simulates the dispersal of larvae as passive, neutrally buoyant particles in the flow field simulated by the ocean model.

The domain of the ocean model is an approximately 200 km × 400 km area that is open on four sides with a layer of the "pretty-good-sponge" developed by Lavelle and Thacker (2008) padded along the inner edge of the boundary to absorb the outgoing baroclinic waves originating from the interior of model domain (Figure 2b). At the outer limit of the sponge layer, derivatives normal to the boundary are set to zero for model velocities, free-surface elevation, temperature, and salinity. The model does not include surface forcing (e.g., winds, eddies, atmospheric pressure, and precipitation) and heat exchange. Bottom friction is introduced in the model as $\overrightarrow{\tau_b} = C_d \left|\overrightarrow{U_0}\right| \overrightarrow{U_0}$, where $\overrightarrow{\tau_b}$ is the bottom stress, $C_d = \mathbf{0.003}$ is the drag coefficient, and $\overrightarrow{U_0}$ is the horizontal velocity within the first model cell above the seafloor. The model domain covers the ridge segment between 8° and 10° N bounded to the north by the Clipperton Transform Fault and to the south by the Siqueros Transform Fault and the Lamont Seamount Chain to the west of ridge segment. The model grid is stretched in horizontal directions so that the finest resolution ($\Delta\mathbf{X} = \mathbf{1108}$ m and $\Delta\mathbf{Y} = \mathbf{1866}$ m) is located on the ridge axis at 104.25°W, 9.69°N. In the vertical direction, the grid is stretched to have the finest resolution ($\Delta\mathbf{Z}$=14 m) at the ridge crest level.

Forcing is determined from measured current meter data taken within the domain interior using the inverse method described in Lavelle et al. (2010), which is summarized as follows. At large distances from the ridge or other topography, the dynamic balance of the large-scale background flow can be approximated as

$$\frac{\partial \overrightarrow{U_{Bkg}}}{\partial t} = -f \times \overrightarrow{U_{bkg}} + \overrightarrow{F_B} \tag{1}$$

where $\overrightarrow{U_{bkg}}$ is the background horizontal velocity, f is the Coriolis coefficient, and $\overrightarrow{F_B}$, the model forcing, is a body force that represents the external forcing (e.g., tides, winds) that drives the background flow within the

modeled region. The inverse procedure starts with taking an initial estimate $\overrightarrow{U_{bkg1}}$ of the background currents and substitute it into equation (1) to obtain $\overrightarrow{F_B}$ for the initial model run. Subsequently, the simulated current time series $\overrightarrow{U_{mod}}$ is recorded at a target location above the ridge where current measurements ($\overrightarrow{U_{obs}}$) are available. The inverse method considers the model to be a Green's function linking, via a convolution in the time domain, $\overrightarrow{U_{bkg}}$ to $\overrightarrow{U_{obs}}$. At tidal and higher frequencies the model is primarily a linear one. The Convolution theorem allows the time domain convolution to be reexpressed in the frequency domain as an algebraic relationship connecting background and target current spectra via the complex model spectrum $\boldsymbol{G}$ in the form

$$\widetilde{U}_{obs}(\omega) = \boldsymbol{G}(\omega)\widetilde{U}_{bkg}(\omega) \tag{2}$$

where $\widetilde{\ }\boldsymbol{U}$ is the complex current spectrum and ω is frequency. Substituting the spectra of $\overrightarrow{U_{bkg1}}$ and $\overrightarrow{U_{mod}}$ into the right- and left-hand sides of equation (2) gives an estimate of $\boldsymbol{G}(\omega)$. This estimate is then substituted back into equation (2) along with the spectrum of the observed currents $\overrightarrow{U_{obs}}$ at the target location to obtain an improved guess of $\overrightarrow{U_{bkg}}$ and $\overrightarrow{F_B}$ (through equation (1)) for a second model run. The same procedures can be repeated iteratively until a satisfactory match between $\overrightarrow{U_{mod}}$ and $\overrightarrow{U_{obs}}$ is achieved at the target location.

In this study, the current-meter data used to derive model forcing were recorded at the location marked in Figure 2b at 2,440 m depth and 128 m above the ridge crest from 9 November 2006 to 25 November 2007. We reduced the amplitudes of measured currents by half and used them as the initial estimate of the background currents. The final forcing was derived iteratively as described in the preceding paragraph after two model runs when the comparison between measured and simulated currents at the aforementioned location demonstrated a reasonable match (Figure S1 in the supporting information).

It is important to note that the inverse procedure described above results in a spatially uniform forcing time series. Despite such simplification, the forcing derived this way has the advantage of including the full spectrum (2-hr to 381-day periods with 1-hr sampling intervals) of flow motions recorded in the current meter data. As a result, the model reasonably well reproduces a number of observations made from current measurements and a tracer release experiment conducted near the ridge axis (Lavelle et al., 2010). On the other hand, the lack of spatial variation in the forcing undoubtedly diminishes the fidelity of the simulated flow field as the distance from the ridge axis grows. With full acknowledgment of this limitation, we primarily focus on the near-ridge dispersal of larvae.

The model used here is a hydrostatic one and is not suitable for simulating the buoyance-driven flows associated with hydrothermal discharge whose core dynamics are nonhydrostatic. Furthermore, the model's horizontal resolution (~1,000 m) is too coarse to resolve the hydrothermal sources on the ridge segment, which are typically concentrated in vent fields $<$100 m across. In addition, in an environment with limited topographic channelization, such as the shallow trough at the crest of EPR, the effects of hydrothermal discharge on flow primarily occur at spatial scales up to a few hundred meters around the source vents (Lavelle, 1997), which are too small to be resolved in our model. Based on these reasons, we chose not to include the buoyancy and turbulent mixing induced by hydrothermal venting in our simulations.

We modified the particle-tracking algorithm developed by Blanton (1995) to make it compatible for coupling with the ocean model. In short, the algorithm calculates 3-D trajectories of a particle based on modeled flow velocities using the fourth-order Runge-Kutta integration scheme with adaptive step size control (Press, 2007). The particles released in the model are neutrally buoyant passive drifters. The bottom boundary is closed so that no particle is lost through the seafloor. At each time step, the algorithm searches for particles whose positions are below the seafloor. Those particles are placed above the seafloor at positions projected from the bottom currents and the slope of topography. The surface and lateral boundaries are open; the algorithm marks a particle that has penetrated one of those boundaries as lost and stops tracking that particle.

Although most vent larvae have limited swimming ability to overcome the ambient currents in horizontal directions, a larva can achieve ontogenetic change in vertical position via directional swimming and/or changes in buoyancy. Entrainment into a rising hydrothermal plume is another way for vent larvae to elevate its vertical position in the water column (Kim et al., 1994; Mullineaux & France, 1995). To take into account the vertical movement of larvae following initial release from the seafloor, we released and tracked particles at 10 m and 225 m above bottom (mab). The near-bottom particles represent larvae that do not move vertically (actively or passively) after they are spawned. The above-bottom particles represent "balloonist" larvae that

Table 1
Coordinates of the 10 Vent Sites Included in the Model

Name	Lon (°W)	Lat (°N)	Cluster
Biovent	104.294	9.850	Northern
EastWall	104.292	9.840	Northern
Bio9	104.291	9.835	Northern
Choo-Choo	104.289	9.827	Northern
TevniaHole	104.288	9.818	Northern
V	104.283	9.787	Middle
A	104.281	9.781	Middle
Hot8	104.279	9.771	Middle
K	104.241	9.496	Southern
PBR500	104.240	9.488	Southern

Note. Each vent site has a nominal area of 1 km × 1 km. For two adjacent sites that are less than 1 km apart, their longitudinal lengths are reduced so there is no overlap between those two sites (in other words, splitting the distance between them.

move upward shortly after spawning via directional swimming, buoyancy, and/or entrainment into buoyant plumes (not explicitly simulated by the model). For a balloonist larva, we neglected horizontal advection during the larva's ascent assuming a relatively short risetime (<1 day) so that the transverse distance is only a small fraction of the total horizontal transport during the larval phase (set to 30 days in the model). Particles were released at both heights every 12 min from the 10 vent sites marked in Figure 2c.

In the model, larvae have no mortality and can settle only after their Tp. Since Tp is poorly constrained for most vent larvae, we used different values (1, 5, and 25 days) to bracket a realistic range of Tp for benthic species and investigate its importance in regulating larval settlement along the ridge axis. This range is consistent with estimates of larval Tps in diverse invertebrate species (Jackson & Strathmann, 1981). A 30-day larval phase duration (PLD) was used in the model based on previous estimates of the larval lifespan of the vent tubeworm *R. pachyptila* (Marsh et al., 2001). Our model does not explicitly resolve the descent of larvae during settlement. Instead, at any time after its Tp, a larva instantaneously settles onto the bottom if it passes over one of the source vent sites (see Figure 2c and Table 1 for their locations and areas). This simplified treatment of larval settlement is not ideal, but our current knowledge of the dynamics involved with the settlement of vent larvae is rudimentary, and hence, it is difficult to model those dynamics without introducing large uncertainties. As a result, we elect to leave more detailed modeling of settlement to future research after more is learned about the settlement behaviors of vent larvae from field and laboratory studies.

4. Model Flow Field

The forcing used to drive model flow was derived from the current measurements made at 128 m above the ridge crest (2,440 m depth) at the location marked in Figure 2b using the inverse procedure described in Lavelle et al. (2010). Comparison between measured and simulated currents at the location of the current meter (Figure 2b) demonstrates a reasonable match with correlation coefficients of 0.92 and 0.83 for the zonal (u) and meridional (v) current components (see Figure S1) over a 354-day period starting from 19 November 2006. The lower correlation coefficient for v is likely because v has much stronger low-frequency oscillations than u, which are difficult to match using the inverse procedure (Lavelle et al., 2010).

Mean circulation is anticyclonic around the ridge segment with a northward flow along the western flank and a southward flow along the eastern flank (Figure 3a). Those flank jets (delimited by the 1-cm s^{-1} contours) extend vertically from the seafloor to 272 and 515 m above the ridge crest and horizontally from the ridge axis to 16 and 27 km toward off-ridge directions on the western and eastern flanks, respectively. The cores of those jets (delimited by the 2.5-cm s^{-1} contours) hug the ridge flanks. Inside those cores, the maximum mean velocity reaches 3 cm s^{-1} for the northward jet and 4 cm s^{-1} for the southward jet. The relative strengths of the flank jets vary with periods of dominating northward flow alternating with periods of dominating southward flow, with maximum instantaneous velocities ~15 cm s^{-1} on both sides of the ridge (Figure S2). When the northward flow dominates, the jet interface moves eastward across the ridge, while the opposite occurs when the southward flow dominates. In some extreme cases, jets on both flanks are in the same direction, although the cross-ridge shear is still anticyclonic (Figure S2). The time-averaged zonal velocity is predominantly westward on the western side of the ridge, whose strength decreases with height off the bottom (Figure 3b). The strongest westward flow (~0.8 cm s^{-1}) occurs next to the western flank of the ridge, and a narrow zone of eastward flow of the same magnitude exists by the eastern flank (Figure 3b). Farther off the ridge, the direction of the zonal flow reverses and becomes westward. Note that the across-ridge and vertical structures of the meridional and zonal flows from our 3-D model differ from the results of the previous 2-D simulation (Figures 2a and 2b in McGillicuddy et al., 2010). The most notable difference is the prominent asymmetry of the 3-D meridional and zonal flows across the ridge, whereas the 2-D results are near symmetric, especially for zonal velocity. In addition, the 3-D flank jets extend to higher altitudes (272 and 515 m above the ridge crest on the western and eastern flanks) than the 2-D jets (192 and 261 m as delimited by 1 cm s^{-1} contours). Two aspects may contribute to the differences between the 3-D and 2-D

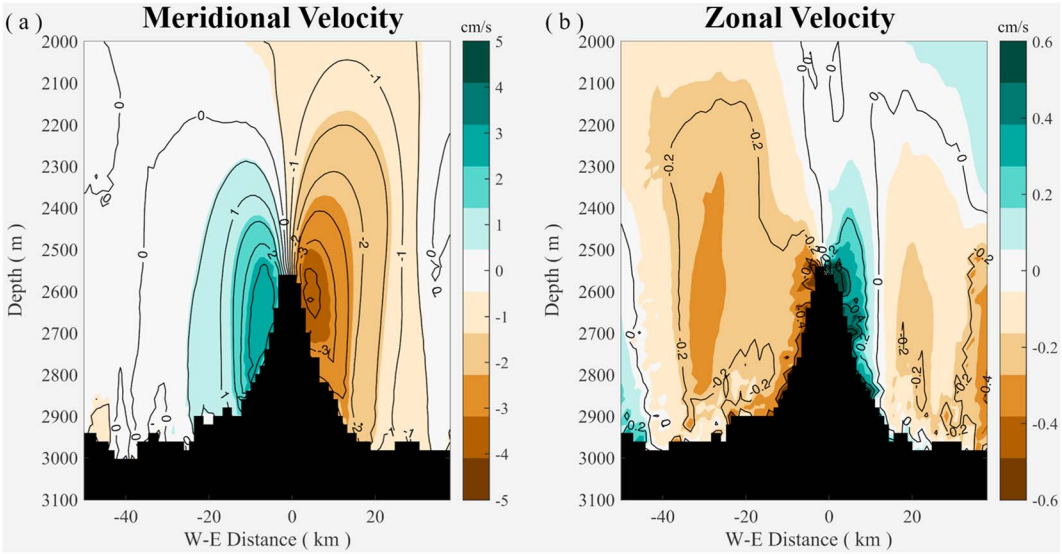

Figure 3. Model (a) meridional and (b) zonal velocities bin averaged in the meridional direction between 9.4°N and 9.8°N and time averaged over a 354-day period starting from 19 November 2006. The *x* coordinate origin is shifted to the ridge crest at *x* = 16 km in Figure 2b.

results. First, the forcing used to drive flows in the 3-D and 2-D simulations was derived from current measurements made at different locations and times. Second and more importantly, the realistic bathymetry used in the 3-D simulation, wherein the ridge is of finite length and asymmetric, differs substantially from the idealized infinitely long axisymmetric ridge used in the 2-D simulation.

The presence of anticyclonically sheared flow with maximum speed ~15 cm s^{-1} across the ridge in our model results is consistent with the current meter observations at the EPR 9°–10°N reported in Liang and Thurnherr (2011). In an earlier study, Cannon and Pashinski (1997) observed similar ridge-trapped flank jets at the Juan de Fuca Ridge at 45°N. Lavelle (2012) investigated the dynamics underlying the flank jets at the EPR using a 2-D model of time-dependent flow over an idealized infinitely long axisymmetric ridge. His results suggested that the jets can arise from topographic rectification of oscillatory flows in a stratified water column. In particular, the nonlinear interactions of oscillatory flows at subinertial frequencies with heat and salt cause the isopycnals to dome over the ridge. The resulting baroclinic pressure gradients, which are in geostrophic balance, drive anticyclonically sheared flow along ridge flanks. The presence of those flank jets at the EPR 9°–10°N can significantly affect the dispersal of larvae from local vent habitats. Because the speed of jets is much higher than that of the westward large-scale mean flow at the EPR (Liang & Thurnherr, 2011), those jets can serve as dispersal expressways for the along-ridge larval transport and strongly affect its spatial-temporal variations, which are discussed in detail in sections 4 and 5.

A zonal snapshot of model flow bin averaged over the central segment between 9.4° and 9.8°N shows near-bottom currents rise over the eastern flank and move downward on the western flank (Figure S3). The horizontal flow direction reverses at times driven by the semidiurnal tidal currents, although the mean flow is westward over the 354-day period starting from 19 November 2006. It is evident that such cross-ridge flow will transport larvae released along the ridge axis off and below the ridge crest to set the stage for the along-ridge dispersal of those larvae in the flank jets discussed above. Also, the direction of the cross-ridge flow at the time of a larva's release will determine the direction of its along-ridge transport. A larva released into westward cross-ridge currents will enter the northward jet on the western flank, while a larva released into eastward currents will enter the southward jet on the eastern flank. Such directional effects are most noticeable for larvae released close to the bottom where the relatively strong cross-ridge flow (Figure S3) can transport larvae off and below the ridge crest (Figure S4) to enter the cores of flank jets where the flows are most robust (Figure 3a).

The flank jets are most robust along the northern part of the ridge segment between the Clipperton Transform Fault and an overlapping spreading center (Macdonald et al., 1988), where an offset of ridge

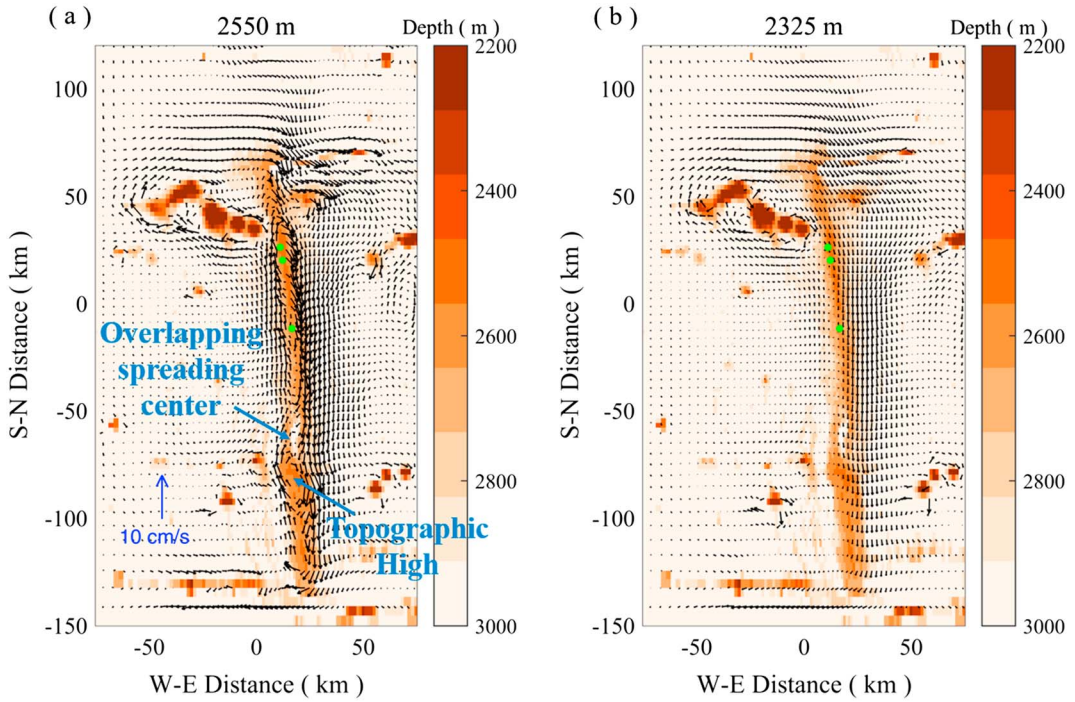

Figure 4. Model flow velocities averaged over a 354-day period starting from 19 November 2006 at (a) 2,550 m (the ridge crest) and (b) 2,325 m (225 m above the ridge crest). The green dots mark the locations of vents: Bio9, A, and K labeled in Figure 2c. The locations of the overlapping spreading center and the local topographic high are labeled.

axis interrupts the axial continuity of the segment (Figure 4a). In addition, the southward jet along the eastern flank is stronger than the northward jet along the western flank. Prominent cross-ridge flows occur near the Clipperton Transform Fault, the overlapping spreading center, a local topographic high to the south of the overlapping spreading center, and the southern end of the ridge segment where it meets the Siqueros Transform Fault. The cross-ridge flows at both ends of the ridge segment along with the flank jets form a clockwise circulation; another noticeable clockwise circulation is present around the Lamont Seamount Chain. In comparison, at 225 m above the ridge, the overall strengths of the flank jets diminish while the southward jet remain stronger than its northward counterpart, and the zonal extent of the southward jet expands westward to cover the ridge axis (Figure 4b). The strength of the cross-ridge flow also diminishes significantly, especially near the overlapping spreading center and local topographic high where no discernible cross-ridge flow is present.

5. General View of Simulated Larval Dispersal Patterns

The complex spatial structure and temporal variation of the regional circulation at the EPR 9°–10°N discussed in section 3 suggests that the larval dispersal patterns near the ridge are likely very different from what one would infer from the large-scale background flow or single-point current measurements made in that region. The probability density functions (PDFs) of larval dispersal patterns calculated from the model as a function of time and space (Figure 5) reflect these complex flows.

For larvae released at 10 mab, their dispersal patterns demonstrate several prominent features. First, the PDFs show removal of larvae from the ridge crest by the cross-ridge flow (Figure S3). Specifically, the percentage of larvae over the ridge (bounded by the 2,800-m depth contour) decreases from near 100% to 45% when the larval travel time increases from 1 to 10 days and ultimately down to 19% at the end of the 30-day larval life-span. Second, the PDFs show distinct peaks along the ridge flanks at 10 days after release (Figure 5e), which likely reflect transport of larvae in the cross-ridge flow (Figure 3b) and their subsequent entrainment into the flank jets (Figure 3a). Those peaks diminish as the travel time increases, especially on the western flank where the ridge-flank peaks all but disappears at 20 days after release (Figure 5g). Third, the zonal dispersal of larvae

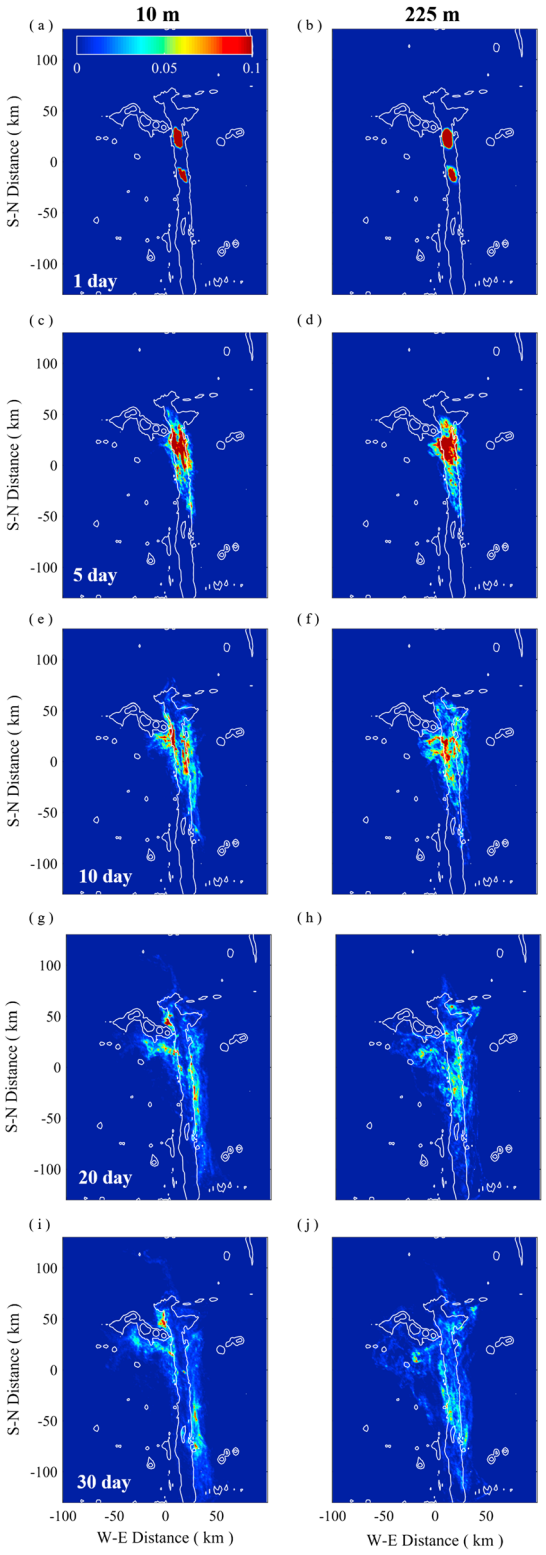

Figure 5. Probability density function (PDF) of larvae released at (left) 10 mab and (right) 225 mab (right) every 12 min from 19 November 2006 to 1 October 2007. To calculate the PDF, the model domain is regrided into 1 km × 1 km bins and the PDF represents the percentage of larvae that occupies each bin at (a and b) 1 day, (c and d) 5 days, (e and f) 10 days, (g and h) 20 days, and (i and j) 30 days after the release.

is primarily westward, which is consistent with the dominant direction of the cross-ridge flow (Figure 3b). Most of those westbound larvae travel along the southern edge of the Lamont Seamount Chain toward its western tip (Figures 5g and 5i). Lastly, few larvae (~1.6%) transit northward of the Clipperton Transform Fault (y ~75 km) by the end of the 30-day larval lifespan, which suggests that the presence of the transform fault impedes northward larval transport from the ridge.

For larvae released at 225 mab, the aforementioned dispersal patterns persist in general despite some noticeable differences. First, the PDFs have less distinctive peaks along the ridge flanks, which suggests that the cross-ridge transport of larvae and their subsequent entrainment into the flank jets decrease at high altitudes (Figure 5f). This is expected as the strengths of both the flank jets and the cross-ridge flow decrease with height above the ridge (Figure 3). Second, the cross-ridge dispersal of larvae is weaker for those released at 225 mab than at 10 mab. For example, the time-averaged zonal dispersal distance decreases from 17 km for larvae released at 10 mab to 14 km for larvae released at 225 mab at the end of the 30-day larval lifespan (Figure S5a). This is expected as the strengh of the zonal flow near the ridge decreases with height off the bottom (Figure 3b). As a result, the balloonist larvae have a better chance of remaining close to the ridge and hence improved odds of local retention than their near-bottom counterparts. Specifically, 36% of the larvae released at 225 mab remain over the ridge axis by the end of the 30-day larval lifespan compared with 19% for larvae released at 10 mab. In contrast, the meridional dispersal distances of larvae released at both heights are similar (Figure S5b) despite the decrease of the strengths of flank jets with height off the bottom. This difference is not present in the 2-D model results, wherein the meridional dispersal distance reduces by half for larvae released at 225 mab relative to 10 mab (McGillicuddy et al., 2010). The difference between the 2-D and 3-D results is due to the following reasons. First, the ridge is of finite length in the 3-D model. The presence of ridge boundaries in the north (the Clipperton Transform Fault) and south (the Siqueros Transform Fault) impede the larval dispersal in the along-ridge directions by limiting the along-ridge length scales of flank jets. In addition, zonal flows near the overlapping spreading center and the local topographic high transport part of the southbound larvae across the ridge to enter the northward jet on the western flank (Figure 5). In comparison, those topographic constraints are absent in the 2-D simulation wherein the ridge is continuous, infinitely long, and invariant in the along-ridge direction. As a result, the dependence of the along-ridge dispersal distance on flank-jet strengths is more evident in the 2-D simulation. Second, as discussed in section 4, the 3-D flank jets extend to higher altitudes above the ridge crest than the 2-D jets, which cause the along-ridge transport for larvae released at 225 mab to be stronger in the 3-D model than in the 2-D one. In addition to the PDFs shown in Figure 5, animations showing the trajectories of larvae released from vents A, Bio9, and K are included in the supporting information (Movies S1 to S3).

6. Flank-Jet-Driven Temporal Variation of Larval Dispersal

The anticyclonically sheared flank jets, which are the most prominent features of the regional circulation at the EPR 9°–10°N, are critical pathways

for the along-ridge transport of larvae. The relative strengths of those jets and their temporal variations substantially affect the larval dispersal patterns. Those effects are evident in comparisons (Figures 6 and 7) of trajectories of larvae released from three vent sites (Bio9, A, and K), each representing one of three vent clusters marked in Figure 2c.

We first examined a period when the northward jet along the western flank is dominant (Figure 6). During this period, the overall larval dispersal direction is northward. For larvae released at 10 mab, most of them initially travel northward along the western flank of the ridge while a smaller number of larvae move southward along the eastern flank. The presence of the Clipperton Transform Fault poses a roadblock to the northbound larvae. While some of those larvae pass over the fault into the northern abyssal plain, the rest stop their northward motion at the fault-ridge intersection and turn eastward to travel along the fault and/or southward to travel down the ridge on its eastern side. In addition, off axis topographic features such as the Lamont Seamount Chain divert part of the northbound larvae away from the ridge. Such diversion is most prominent for larvae released at the southern vent site K, from which most larvae are deflected westward to travel along the southern edge of the Lamont Seamount Chain (Figure 6e). For larvae that initially travel southward along the eastern flank, all of them cross the ridge within 50 km of their natal sites and travel northward on the western side of the ridge. The overall dispersal patterns of larvae released at 225 and 10 mab are similar. The most noticeable difference is more larvae from vent A disperse westward off the southern edge of the Lamont Seamount Chain at 225 mab than at 10 mab (Figure 6d).

When the southward jet on the eastern flank becomes dominant, such reversal of the relative strengths of flank jets leads to drastic changes in larval dispersal patterns and a north-to-south shift of the overal dispersal direction (Figure 7). For larvae released at 10 mab, most of them initially travel southward along the eastern flank, while a smaller number of larvae move northward along the western flank. For larvae released at the northern vent sites (Bio9 and A), such ridge-crossing and turning occurs at three locations: (1) midway between the overlapping spreading center and the natal site, (2) at the overlapping spreading center, and (3) around the southern edge of the local topographic high (Figures 7a and 7c). For larvae released at the southern vent site K, the southbound larvae gradually deviate away from the ridge to the east and start turning westward when they approach the Siqueros Transform Fault (Figure 7e). For larvae that initially travel northward, almost all of those released at Bio9 and A are deflected to the west and then travel southward at the gap between the ridge and the Lamont Seamount Chain (Figures 7a and 7c). In comparison, almost all northbound larvae from K cross the ridge within 25 km and then travel southward along the eastern flank of the ridge (Figure 7e). For larvae released at 225 mab, the southbound larvae from Bio9 and A are located farther west, which is likely because the zonal extent of the southward jet expands to cover the ridge axis at 225 mab (Figure 4b). In addition, larvae released from K at 225 mab have enhanced cross-ridge transport near the southern end of the ridge segment. After crossing the ridge, those larvae travel northward along the western flank, and some of them have remarkably returned to the vicinity of K by the end of their 30-day lifespan (Figure 7f).

7. Topographic Constraints on Larval Dispersal

The results shown in Figures 5–7 suggest that seafloor topography has substantial influences on the dispersal of larvae originating from the habitats along EPR 9°–10°N, as mediated by local flow fields. First, the interaction of ridge topography with background currents creates rectified flows along the ridge (i.e., flank jets), which steer larvae to disperse in the along-ridge directions. Second, the presence of the Clipperton and Siqueros Transform Faults imposes topographic constraints on the transport of larvae to neighboring ridge segments. The Clipperton Transform Fault poses a barrier to the northward dispersal of larvae because the mean flow is primarily southward across the fault and eastward along the fault, which prohibits crossing of the northbound larvae (Figure 4a). As a result, the majority of larvae (all but 2%) released from the ridge remain on the southern side of the fault by the end of their 30-day lifespan (Figure 5). For the southbound larvae, their dispersal is impeded by the presence of cross-ridge flows near the Siqueros Transform Fault and less prominent topographic features such as the overlapping spreading center and the local topographic high (Figures 4 and 7). Lastly, the presence of an overall anticyclonic circulation around the ridge segment favors overall near-ridge dispersal (Figures 4 and 5).

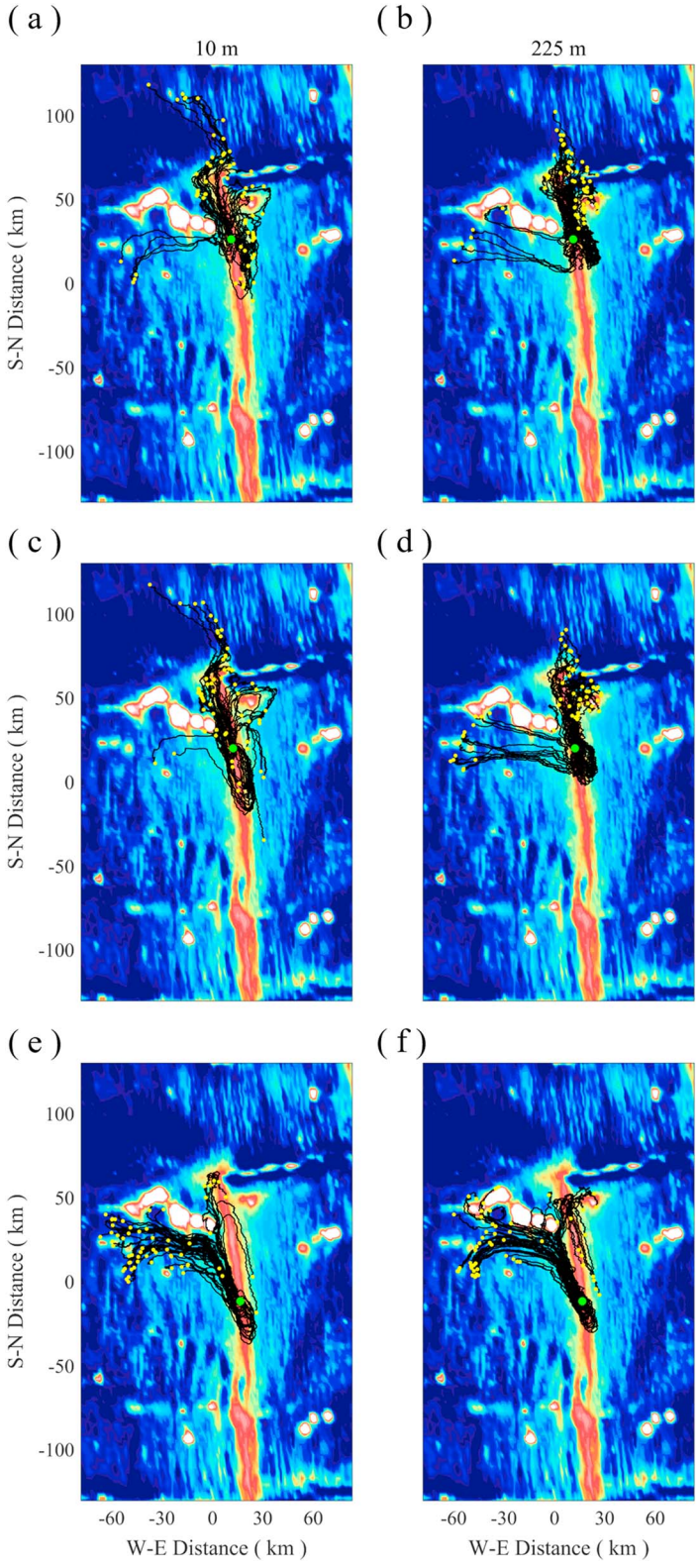

Figure 6. Dispersal trajectories of larvae released at (left) 10 mab and (right) 225 mab from (a and b) Bio9, (c and d) A, and (e and f) K vents over the 30-day planktonic larval duration (PLD). The larvae are released every 12 hr from 9 February to 11 March 2007. This time range is chosen so that at least 50% of the larvae's 30-day planktonic lifetime coincides with a period of dominant northward ridge-flank jets (24 February to 26 March 2007). In each panel, the green dot marks the location of larval source and the yellow dots mark the locations of larvae at the end of their 30-day PLD.

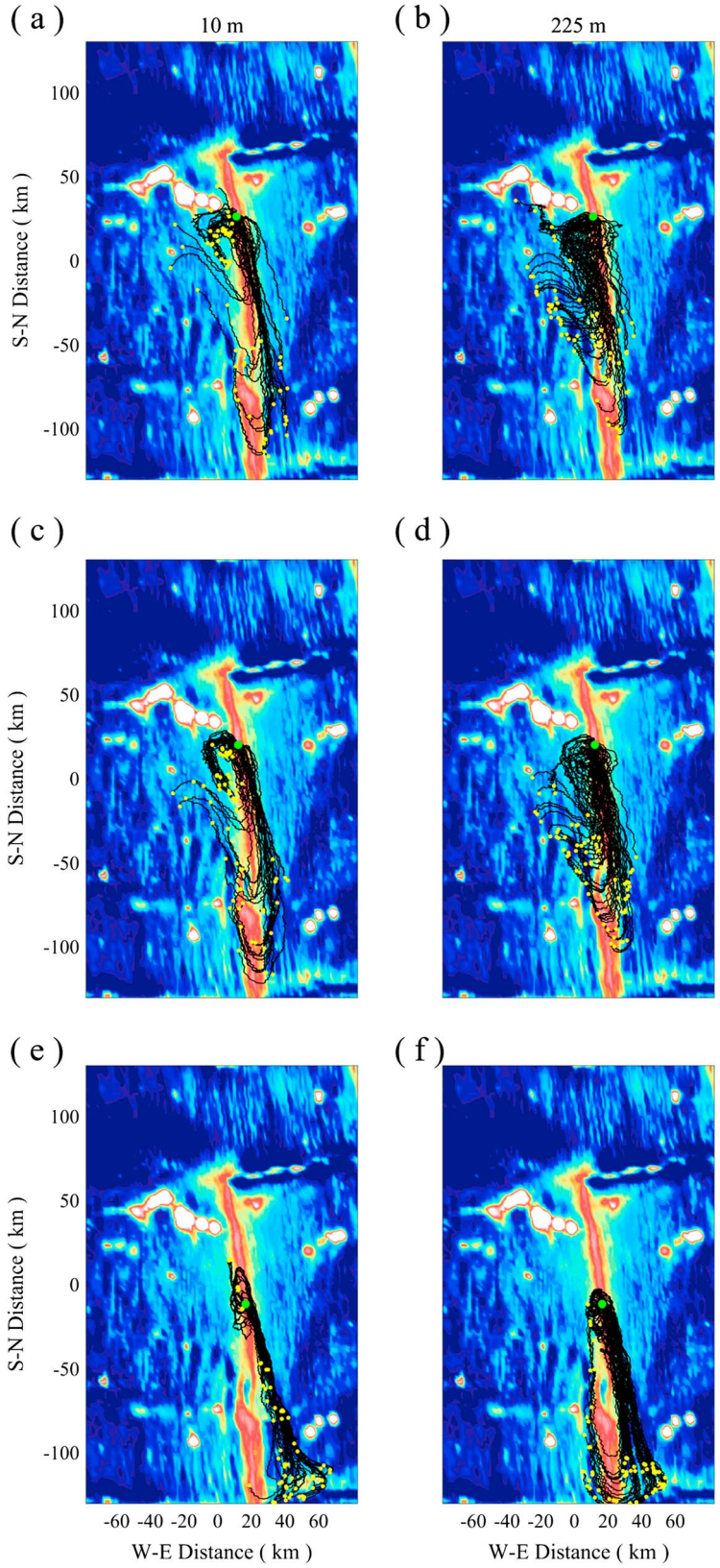

Figure 7. Same as Figure 6 except for larvae released from 28 June to 29 July 2007. This time range is chosen so that at least 50% of the larvae's 30-day planktonic lifetime coincides with a period of dominant southward ridge-flank jets (13 Jul to 13 August 2007).

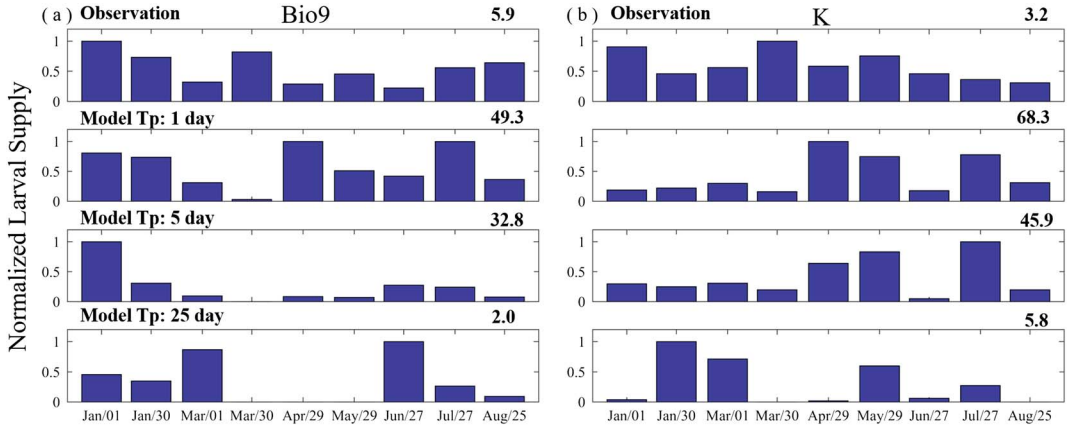

Figure 8. Comparison between observed and model larval supplies at (a) L1 and (b) L2. Larvae are released at 10 mab in the model with precompetency periods of 1, 5, and 25 days. All observed or model time series are normalized by their respective maxima (labeled) in unit larvae/m^2/d for observations or larvae/km^2/d for model results. Collection intervals are 29- to 30-day periods centered at the labeled dates.

Flows near the Lamont Seamount Chain divert northward-moving larvae off the ridge axis to the west (Figure 4). Such dispersal trajectories suggest that larvae spawned from the EPR 9°–10°N can potentially settle onto Lamont seamounts should they host suitable habitats. Although previous seafloor surveys discovered no active venting, those surveys found evidence of relatively young volcanic activities at Lamont seamounts, which suggests that some of them may be hydrothermally active and habitable for vent organisms (Fornari et al., 1988). If this is true, the model dispersal trajectories suggest that the ridge-to-seamount larval supply is most common for larvae released from the southern vent cluster when the northward jet dominates (Figures 6e and 6f).

8. Larval Supply at EPR 9°–10°N

In order to investigate the temporal variation of larval supply at the EPR 9°–10°N and its correspondence to hydrodynamic processes, we compared the total supply (pooled across taxa) estimated from the sediment trap data collected near Bio9 and K vents (Table S1) with the model predictions (Figures 8 and 9). The temporal variation in observed supply showed similar trends between the two sites during the first 7 months of the series (Figure 8), although this correlation was not significant ($r = 0.42$, $P = 0.35$). The trends in the last 3 months of the series were opposing. The mean observed supply over the full time series was greater at Bio9 (3.0 larvae d^{-1} m^{-2}) than at K vent (1.8 larvae d^{-1} m^{-2}).

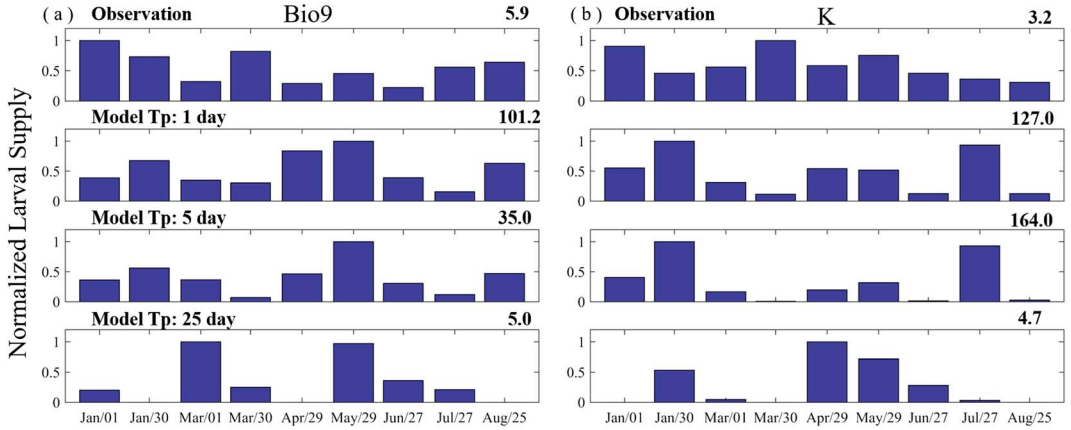

Figure 9. Same as Figure 8 except for larvae released at 225 mab.

Temporal patterns in modeled supply did not correlate with those in observed supply at either site, for any of the Tps (Tp = 1 to 25 days), at either the 10 mab (Figure 8) or 225 mab (Figure 9) release height (see Tables S2 and S3 for correlation statistics for all six Tp periods). The modeled supplies are greater at K than at Bio9 across all Tps and for both release heights (Figures 8 and 9). The modeled supply at both sites was significantly higher for larvae released at 225 mab than at 10 mab, while the total supply decreased with increasing Tp for both release heights.

There are a number of factors that may contribute to the lack of correlation in the simulated and observed time series of larval settlement. First of all, the modeled currents may not be accurate enough to deterministically simulate larval transport. Despite the realistic geometry, high resolution, and data-driven inference of the hindcast forcing, the model does not resolve all of the wide range in spatial and temporal scales potentially relevant to this problem. Moreover, temporal fluctuations in spawning are not represented by our highly idealized biological model, nor is their potential covariance with hydrodynamic conditions favorable for larval retention—which may be a highly episodic process.

In addition, given the striking variation in temporal patterns in modeled supply of larvae between different Tps and release heights, we would expect a strong correlation between observed and modeled supply only if the observed larvae all had the same Tp and dispersed at the same altitude. In our mixed-species observations (Table S1), this certainly is not the case. We collected some species expected to have short Tps (e.g., archaeogastropod limpets) as well as others (the snail *Bathymargarites symplector* and the mussel *B. thermophilus*) that transition into a planktonic feeding stage and may have extended Tps. Although it was tempting to compare the temporal supply patterns of individual species to the modeled supply, we did not attempt to do so because of the low numbers of individuals in each species. Similarly, we did not attempt to pool larvae into Tp categories because of uncertainties in the larval development time scales for most species.

Another possible explanation for the lack of correspondence between the model and the observations is that larval supply at colonized sites may be largely dominated by recruitment from the natal site and relatively unaffected by the hydrodynamically mediated dispersal we modeled in this system. For example, many vent gastropods have no detectable development stages and may be competent upon release or shortly thereafter (Lutz et al., 1986). The supply of species with a Tp shorter than 1 day is not captured by our model. Furthermore, if larval supply comes mostly from the natal site, temporal variations in the supply would reflect primarily the variations of source conditions (e.g., larval spawning rate), which are not included in the model. This scenario would be expected to occur in active, inhabited vents (stage 3 in Figure 1), but not active uninhabited vents (stage 2), suggesting that the primary physical drivers of colonization change substantially over the course of faunal succession at vents.

9. Population Connectivity at EPR 9°–10°N

Our model tracks the dispersal and settlement of a large number of larvae released from 10 vent sites along the EPR 9°–10°N (Figure 2c). Synthesis of model results yielded connectivity matrices as functions of Tp and release height (Figure 10). As commonly used in shallow-water ecological studies (Mitarai et al., 2009; Paris et al., 2007, 2013), the connectivity matrix quantifies larval transport between source and recipient sites. Our results suggest the larval connectivity among the 10 ridge-crest habitats is strongly dependent on Tp and release height.

For larvae released at 10 mab, a short Tp (1 day) corresponds to dominant connectivity among local and neighboring sites (Figure 10a). This is because most larvae are still close to their natal sites when those larvae first reach competency (Figures 5a and 5b). On the other hand, the short Tp prohibits connectivity between two remotely located sites so that few larvae released from the Southern vent cluster settle onto the northern and middle clusters and vice versa. When Tp increases from 1 to 5 days, the connectivity matrix shows an overall north-to-south trend in larval supply (in other words larvae primarily settle to the south of their natal sites; Figure 10c). This is likely because the southward flank jet is stronger than the northward jet (Figure 3a), which favors southward larval dispersal. The northern and southern clusters stand out in the connectivity matrix as the dominant source and recipient, respectively, of larvae. When Tp increases to 25 days, the north-to-south trend in larval supply becomes less prominent with relatively more larvae settling to the north of their natal sites (Figure 10e).

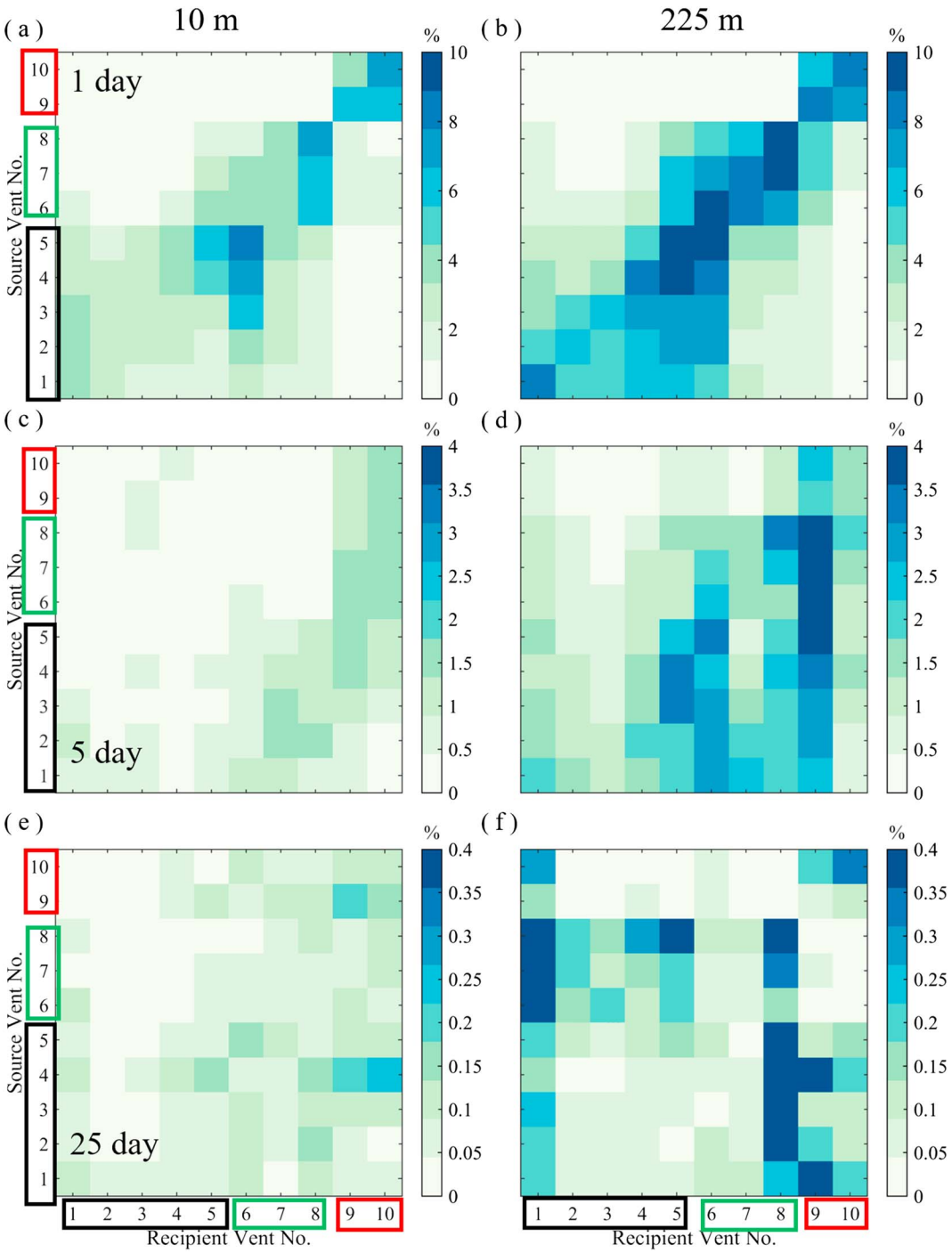

Figure 10. Connectivity matrices of the 12 model vent sites for larvae released at (left) 10 mab and (right) 225 mab every 12 min from 19 November 2006 to 1 October 2007. Panels in each row correspond to a precompetency period of (a and b) 1 day, (c and d) 5 days, and (e and f) 25 days. Note that the color scale varies among precompetency periods for graphic clarity. The vents in the northern, middle, and southern groups are enclosed in black, green, and red boxes, respectively.

For larvae released at 225 mab, the connectivity matrices have similar overall patterns as those for larvae released at 10 mab. The most noticeable difference is that the overall settlement success rates (percentage of larvae that settle) are significantly higher for larvae released at 225 mab than at 10 mab. For example, when Tp equals 1 day, 37% of larvae released at 225 mab settle successfully compared with 22% for those released at 10 mab. When Tp increases to 5 days, the success rates decrease to 16% and 6% for larvae released at 225

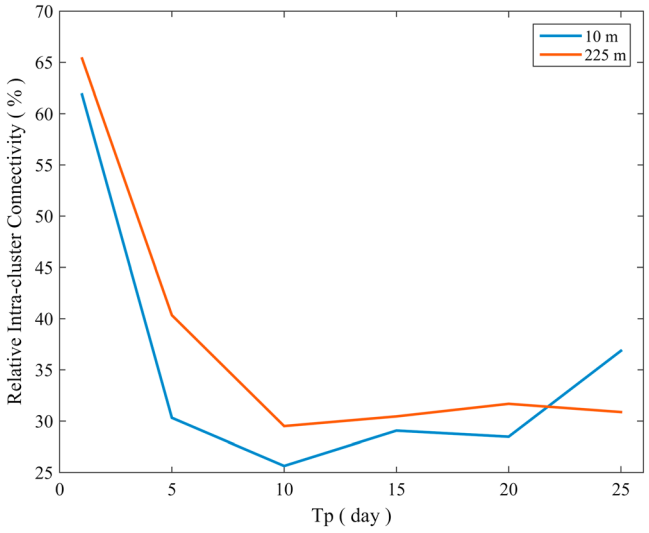

Figure 11. Intracluster connectivity (percentage of the total larval settlement rate that is accounted for by larvae that settle within their natal vent clusters) of larvae released at 10 mab (blue) and 225 mab (red).

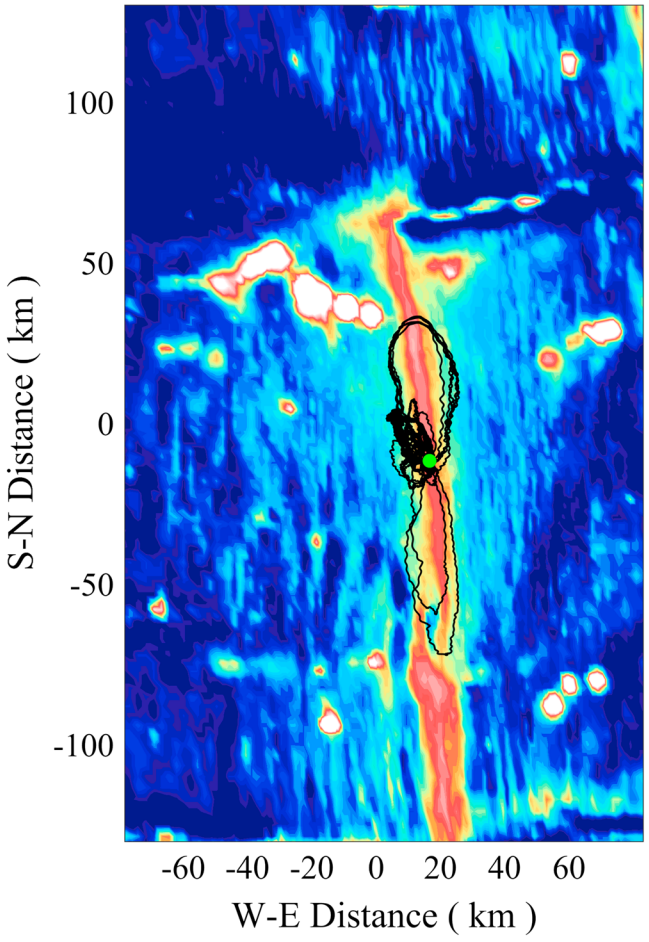

Figure 12. Dispersal trajectories of larvae released from K vent at 10 mab every 12 min from 19 November 2006 to 1 October 2007 that return and settle onto the natal site after a 25-day precompetency period.

and 10 mab, respectively. Those rates further decrease to 3.5% and 1.5% when Tp increases to 20 days. The decrease in larval settlement success rate with increasing Tp for both release heights suggests that a short Tp favors recolonization of larvae within the ridge-crest habitats, which are relatively closely spaced so that the inter-vent distance can be smaller than the precompetent dispersal distance. On the other hand, the increase of larval settlement success rate with release height is primarily because the strengths of cross-ridge flows decrease with height off the bottom (Figure 3b). Therefore, balloonist larvae have reduced off-ridge transport and hence improved odds of settlement onto the ridge-crest habitats than larvae that stay near the bottom. This is also consistent with the finding from previous 2-D simulations (McGillicuddy et al., 2010).

We further investigate the relative importance of connectivity among neighboring and remote sites by calculating the relative intracluster connectivity, which is the percentage of the overall larval settlement rate that is accounted for by larvae that settle within their natal clusters. The results show a sharp decrease of intracluster connectivity: from 62% to 26% for larvae released at 10 mab and from 65% to 30% for larvae released at 225 mab as Tp increases from 1 to 10 days (Figure 11). Thus, a short Tp favors connectivity among local and neighboring sites. However, we note that intracluster connectivity shows a slight increase as Tp extends from 10 to 25 days (Figure 11). Our interpretation for this increase is, for Tp $>$ 10 days, the prolonged travel time allows some larvae that have been transported far from their natal clusters to return to those areas. The presence of such reconnecting larval trajectories (Figure 12) over a relative long travel time is likely facilitated by the anticyclonically sheared flank jets and cross-ridge flows that vary in space and time.

10. Summary

Numerical larvae were tracked in a realistic 3-D hydrodynamic environment to investigate dispersal and connectivity among 10 ridge-crest habitats of the EPR 9–10°N segment. The following are major findings:

First, the simulated hydrodynamic environment at the EPR 9–10°N segment features topographically influenced flows with complex spatial-temporal variations that differ substantially from the large-scale background flow. Most noticeably, modeled flows are amplified near the ridge and anticyclonically sheared across the ridge axis in the meridional directions. Those flank jets are critical pathways for the along-ridge transport of larvae, and the relative strengths of those jets substantially affect the patterns of near-ridge larval dispersal.

Second, the model results suggest that the transform faults bounding the ridge segment and off axis topography (the Lamont Seamount Chain) act as topographic barriers to larval dispersal in the along-ridge direction. Furthermore, the presence of an overlapping spreading center and an adjacent local topographic high impedes the southward along-ridge larval transport. The deflection of flows from along-ridge to cross-ridge directions at those topographic barriers, along with the flank jets, forms anticyclonic circulations in between those barriers.

Third, modeled larval supplies and connectivity within ridge-crest habitats are sensitive to larval Tps and release heights. The overall recolonization rate is substantially higher for larvae having a short Tp and dispersing at a high altitude. Both of these factors result in reduced cross-ridge

dispersal distances and hence an increased likelihood for larvae to be close to the ridge-crest habitats by the end of the Tp. In addition, a short Tp favors connectivity among local and neighboring habitats. More interestingly, for larvae having a long Tp (>10 days), the prolonged travel time allowed some of those larvae to return to their natal vent clusters, which results in an unexpected increase of connectivity among natal and neighboring sites. Such returns would have been all but impossible if the near-ridge currents were nearly spatially uniform as the large-scale background flow in the region.

Lastly, the strong influence of Tps on larval recolonization and connectivity suggests that model-based predictions of larval supply and connectivity may be difficult to interpret when Tps are unknown. Measurements of Tp exist for only a few vent species, suggesting that this should be a key objective for future biological studies. In addition, the sensitivity of modeled supplies and connectivity to release height emphasizes the importance of knowing the vertical movements of larvae when studying their dispersal in a hydrodynamic environment such as the EPR 9–10°N that features prominent vertically sheared flows.

11. Implications for Long-Distance Larval Dispersal

The modeled dispersal patterns suggest that the topographical barriers (e.g., transform faults) at the ends of the ridge segment impede long-distance (a few hundred kilometers), cross-segment larval dispersal. The maximum dispersal distances of larvae released at 10 and 225 mab are 162 and 137 km at the end of the 30-day PLD. Out of 378,860 larvae released at 10 mab, fewer than 3% of those larvae have reached beyond 120 km of their source vents. This percentage decreases to less than 1% for larvae released at 225 mab. These results suggest the long-distance (~300 km) larval dispersal observed in Mullineaux et al. (2010) is likely rare and potentially driven by physical processes not included explicitly in this model. Adams et al. (2011) and Adams and Flierl (2010) suggest that complex interactions with mid-ocean eddy fields may create intensified deep currents that extend many hundreds of kilometers for periods of weeks, potentially providing a conduit for larval exchange between ridge segments, effectively overriding the hydrodynamic barriers we describe here at the ends of segment. On the other hand, even with enhanced deep currents induced by surface eddies, the estimated travel time for dispersal over a few hundred kilometers would still likely exceed the 30-day PLD we use. Longer travel times for some species may be possible, as some gastropod larvae have surprisingly long planktonic durations (months to years; e.g., Strathmann & Strathmann, 2007), and a few other vent species have larvae with the potential to persist longer than 30 days in the plankton (Miyake et al., 2006; Watanabe et al., 2004). The effects of eddies on abyssal flow cannot be simulated explicitly by our model since its forcing is spatially uniform. Our future research will focus on adapting the current model by incorporating spatially varying forcing through lateral and surface boundary conditions and simulating the effects of surface-generated eddies on long-distance larval dispersal at EPR.

Acknowledgments

The sediment-trap data presented in this paper are included in Table S1. The bathymetric data used in the model can be downloaded from the Global Multi-Resolution Topography (GMRT) Synthesis of Marine Geoscience Data System (MGDS) (https://www.gmrt.org/GMRTMapTool). The ocean current time series data used in this work were acquired in 2006-2007 by Andreas Thurnherr at the Earth Institute of Columbia University. Those data can be accessed in the supporting information. D.J. McGillicuddy gratefully acknowledges support from the National Science Foundation and the Holger W. Jannasch and Columbus O'Donnell Iselin Shared Chairs for Excellence in Oceanography. L.S. Mullineaux acknowledges with gratitude support from the National Science Foundation and the Woods Hole Oceanographic Institution (WHOI) Ocean life fellowship. We appreciate the operation support from the Captain and crew of R/V *Atlantis* and the Alvin submersible group. We are thankful to V.K. Kosnyrev for developing the coupling interface between the ocean-circulation and particle-tracking models. We are grateful to J.W. Lavelle for his intellectual support for the modeling work presented in this paper. We thank Houshuo Jiang for sponsoring our use of the cluster computer at WHOI.

References

Adams, D. K., & Flierl, G. R. (2010). Modeled interactions of mesoscale eddies with the East Pacific Rise: Implications for larval dispersal. *Deep Sea Research Part I: Oceanographic Research Papers*, *57*(10), 1163–1176. https://doi.org/10.1016/j.dsr.2010.06.009

Adams, D. K., McGillicuddy, D. J., Zamudio, L., Thurnherr, A. M., Liang, X., Rouxel, O., et al. (2011). Surface-generated mesoscale eddies transport deep-sea products from hydrothermal vents. *Science*, *332*(6029), 580–583. https://doi.org/10.1126/science.1201066

Adams, D. K., & Mullineaux, L. S. (2008). Supply of gastropod larvae to hydrothermal vents reflects transport from local larval sources. *Limnology and Oceanography*, *53*(5), 1945–1955. https://doi.org/10.4319/lo.2008.53.5.1945

Beaulieu, S. E., Mullineaux, L. S., Adams, D. K., & Mills, S. W. (2009). Comparison of a sediment trap and plankton pump for time-series sampling of larvae near deep-sea hydrothermal vents. *Limnology and Oceanography: Methods*, *7*, 235–248.

Blanton, B. O. (1995). DROG3D: User's manual for 3-dimensional drogue tracking on a finite element grid with linear finite elements. Program in Marine Sciences, University of North Carolina, Chapel Hill.

Cannon, G. A., & Pashinski, D. J. (1997). Variations in mean currents affecting hydrothermal plumes on the Juan de Fuca Ridge. *Journal of Geophysical Research*, *102*, 24,965–24,976. https://doi.org/10.1029/97JC01910

Carbotte, S. M., & Macdonald, K. C. (1994). Comparison of seafloor tectonic fabric at intermediate, fast, and super fast spreading ridges: Influence of spreading rate, plate motions, and ridge segmentation on fault patterns. *Journal of Geophysical Research*, *99*(B7), 13,609–13,631.

Fornari, D. J., Perfit, M. R., Allan, J. F., Batiza, R., Haymon, R., Barone, A., et al. (1988). Geochemical and structural studies of the Lamont seamounts: Seamounts as indicators of mantle processes. *Earth and Planetary Science Letters*, *89*(1), 63–83. https://doi.org/10.1016/0012-821X(88)90033-7

Haymon, R. M., Fornari, D. J., Von Damm, K. L., Lilley, M. D., Perfit, M. R., Edmond, J. M., et al. (1993). Volcanic eruption of the mid-ocean ridge along the East Pacific Rise crest at 9 45–52′N: Direct submersible observations of seafloor phenomena associated with an eruption event in April, 1991. *Earth and Planetary Science Letters*, *119*(1–2), 85–101. https://doi.org/10.1016/0012-821X(93)90008-W

Jackson, G. A., & Strathmann, R. R. (1981). Larval mortality from offshore mixing as a link between precompetent and competent periods of development. *The American Naturalist*, *118*(1), 16–26. https://doi.org/10.1086/283797

Khripounoff, A., Comtet, T., Vangriesheim, A., & Crassous, P. (2000). Near-bottom biological and mineral particle flux in the lucky strike hydrothermal vent area (Mid-Atlantic Ridge). *Journal of Marine Systems*, *25*(2), 101–118. https://doi.org/10.1016/S0924-7963(00)00004-X

Kim, S. L., Mullineaux, L. S., & Helfrich, K. R. (1994). Larval dispersal via entrainment into hydrothermal vent plumes. *Journal of Geophysical Research*, *99*, 12,655–12,665. https://doi.org/10.1029/94JC00644

Lavelle, J. W. (1997). Buoyancy-driven plumes in rotating, stratified cross flows: Plume dependence on rotation, turbulent mixing, and cross-flow strength. *Journal of Geophysical Research*, *102*(C2), 3405–3420.

Lavelle, J. W. (2012). On the dynamics of current jets trapped to the flanks of mid-ocean ridges. *Journal of Geophysical Research*, *117*, C07002. https://doi.org/10.1029/2011JC007627

Lavelle, J. W., & Thacker, W. C. (2008). A pretty good sponge: Dealing with open boundaries in limited-area ocean models. *Ocean Modelling*, *20*(3), 270–292. https://doi.org/10.1016/j.ocemod.2007.10.002

Lavelle, J. W., Thurnherr, A. M., Ledwell, J. R., McGillicuddy, D. J., & Mullineaux, L. S. (2010). Deep ocean circulation and transport where the East Pacific Rise at 9–10 N meets the Lamont seamount chain. *Journal of Geophysical Research*, *115*, C12073. https://doi.org/10.1029/2010JC006426

Liang, X., & Thurnherr, A. M. (2011). Subinertial variability in the deep ocean near the East Pacific Rise between 9° and 10°N. *Geophysical Research Letters*, *38*, L06606. https://doi.org/10.1029/2011GL046675

Lutz, R. A., Bouchet, P., Jablonski, D., Turner, R. D., & Warén, A. (1986). Larval ecology of mollusks at deep-sea hydrothermal vents. *American Malacological Bulletin*, *4*(1), 49–54.

Macdonald, K. C., Fox, P. J., Perram, L. J., Eisen, M. F., Haymon, R. M., Miller, S. P., et al. (1988). A new view of the mid-ocean ridge from the behaviour of ridge-axis discontinuities. *Nature*, *335*(6187), 217–225. https://doi.org/10.1038/335217a0

Marsh, A. G., Mullineaux, L. S., Young, C. M., & Manahan, D. T. (2001). Larval dispersal potential of the tubeworm Riftia pachyptila at deep-sea hydrothermal vents. *Nature*, *411*(6833), 77–80. https://doi.org/10.1038/35075063

McGillicuddy, D. J. Jr., Lavelle, J. W., Thurnherr, A. M., Kosnyrev, V. K., & Mullineaux, L. S. (2010). Larval dispersion along an axially symmetric mid-ocean ridge. *Deep Sea Research Part I: Oceanographic Research Papers*, *57*(7), 880–892. https://doi.org/10.1016/j.dsr.2010.04.003

Metaxas, A. (2004). Spatial and temporal patterns in larval supply at hydrothermal vents in the Northeast Pacific Ocean. *Limnology and Oceanography*, *49*(6), 1949–1956. https://doi.org/10.4319/lo.2004.49.6.1949

Mills, S. W., Beaulieu, S. E., & Mullineaux, L. S. (2009). Photographic identification guide to larvae at hydrothermal vents (108 pp.). Woods Hole Oceanographic Institution Technical Report WHOI-2009-05.

Mitarai, S., Siegel, D. A., Watson, J. R., Dong, C., & McWilliams, J. C. (2009). Quantifying connectivity in the coastal ocean with application to the Southern California Bight. *Journal of Geophysical Research*, *114*, C10026. https://doi.org/10.1029/2008JC005166

Mitarai, S., Watanabe, H., Nakajima, Y., Shchepetkin, A. F., & McWilliams, J. C. (2016). Quantifying dispersal from hydrothermal vent fields in the Western Pacific Ocean. *Proceedings of the National Academy of Sciences*, *113*(11), 2976–2981.

Miyake, H., Tsukahara, J., Hashimoto, J., Uematsu, K., & Maruyama, T. (2006). Rearing and observation methods of vestimentiferan tubeworm and its early development at atmospheric pressure. *Cahiers de Biologie Marine*, *47*(4), 471.

Mullineaux, L. S., Adams, D. K., Mills, S. W., & Beaulieu, S. E. (2010). Larvae from afar colonize deep-sea hydrothermal vents after a catastrophic eruption. *Proceedings of the National Academy of Sciences*, *107*(17), 7829–7834.

Mullineaux, L. S., & France, S. C. (1995). Dispersal mechanisms of deep-sea hydrothermal vent fauna. In S. E. Humphris, R. A. Zierenberg, L. S. Mullineaux, & R. E. Thomson (Eds.), *Seafloor hydrothermal systems: Physical, chemical, biological, and geological interactions*, *Geophysical Monograph Series* (Vol. 91, pp. 408–424). Washington, DC: American Geophysical Union.

Mullineaux, L. S., Le Bris, N., Mills, S. W., Henri, P., Bayer, S. R., Secrist, R. G., et al. (2012). Detecting the influence of initial pioneers on succession at deep-sea vents. *PLoS One*, *7*(12), e50015. https://doi.org/10.1371/journal.pone.0050015

Mullineaux, L. S., Mills, S. W., Sweetman, A. K., Beaudreau, A. H., Metaxas, A., & Hunt, H. L. (2005). Vertical, lateral and temporal structure in larval distributions at hydrothermal vents. *Marine Ecology Progress Series*, *293*, 1–16. https://doi.org/10.3354/meps293001

Neubert, M. G., Mullineaux, L. S., & Hill, M. F. (2006). Marine Metapopulations. In *A metapopulation approach to interpreting diversity at deep-sea hydrothermal vents* (pp. 321–350). Boston, MA: Elsevier Academic Press.

Paris, C. B., Chérubin, L. M., & Cowen, R. K. (2007). Surfing, spinning, or diving from reef to reef: Effects on population connectivity. *Marine Ecology Progress Series*, *347*, 285–300. https://doi.org/10.3354/meps06985

Paris, C. B., Helgers, J., Van Sebille, E., & Srinivasan, A. (2013). Connectivity modeling system: A probabilistic modeling tool for the multi-scale tracking of biotic and abiotic variability in the ocean. *Environmental Modelling & Software*, *42*, 47–54. https://doi.org/10.1016/j.envsoft.2012.12.006

Perfit, M. R., & Chadwick, W. W. (1998). Magmatism at mid-ocean ridges: Constraints from volcanological and geochemical investigations. In W. Roger Buck, et al. (Eds.), *Faulting and magmatism at mid-ocean ridges*, *Geophysical Monograph Series* (Vol. 106, pp. 59–115). Washington, DC: American Geophysical Union.

Press, W. H. (2007). *Numerical recipes 3rd edition: The art of scientific computing* (Chap. 17, pp. 907–921). Cambridge, UK: Cambridge University Press.

Ryan, W. B., Carbotte, S. M., Coplan, J. O., O'Hara, S., Melkonian, A., Arko, R., et al. (2009). Global multi-resolution topography synthesis. *Geochemistry, Geophysics, Geosystems*, *10*, Q03014. https://doi.org/10.1029/2008GC002332

Shanks, A. L. (1995). Mechanisms of cross-shelf dispersal of larval invertebrates and fish. In L. R. McEdward (Ed.), *Ecology of marine invertebrate larvae* (pp. 323–367). Boca Raton, FL: CRC Press, Inc.

Soule, S. A., Fornari, D. J., Perfit, M. R., & Rubin, K. H. (2007). New insights into mid-ocean ridge volcanic processes from the 2005–2006 eruption of the East Pacific Rise, 9 46′ N–9 56′ N. *Geology*, *35*(12), 1079–1082. https://doi.org/10.1130/G23924A.1

Strathmann, M. F., & Strathmann, R. R. (2007). An extraordinarily long larval duration of 4.5 years from hatching to metamorphosis for teleplanic veligers of Fusitriton oregonensis. *The Biological Bulletin*, *213*(2), 152–159. https://doi.org/10.2307/25066631

Todd, C. D., Phelan, P. J. C., & Weinmann, B. E. (2006). Improvements to a passive trap for quantifying barnacle larval supply to semi-exposed rocky shores. *Journal of Experimental Marine Biology and Ecology*, *332*(2), 135–150. https://doi.org/10.1016/j.jembe.2005.11.013

Tolstoy, M., Cowen, J. P., Baker, E. T., Fornari, D. J., Rubin, K. H., Shank, T. M., et al. (2006). A sea-floor spreading event captured by seismometers. *Science*, *314*(5807), 1920–1922. https://doi.org/10.1126/science.1133950

Vic, C., Gula, J., Roullet, G., & Pradillon, F. (2018). Dispersion of deep-sea hydrothermal vent effluents and larvae by submesoscale and tidal currents. *Deep Sea Research Part I: Oceanographic Research Papers*, *133*, 1–18. https://doi.org/10.1016/j.dsr.2018.01.001

Watanabe, H., Kado, R., Tsuchida, S., Miyake, H., Kyo, M., & Kojima, S. (2004). Larval development and intermoult period of the hydrothermal vent barnacle Neoverruca sp. *Journal of the Marine Biological Association of the United Kingdom*, *84*(4), 743–745. https://doi.org/10.1017/S0025315404009841h